ACS APPLIED MATERIALS & INTERFACES

www.acsami.org Research Article

How the Interplay between SnO_2 and Zn(II) Porphyrins Impacts on the Electronic Features of Gaseous Acetone Chemiresistors

Francesca Tessore, Eleonora Pargoletti,* Gabriele Di Carlo, Cecilia Albanese, Raffaella Soave, Mario Italo Trioni, Federica Marelli, and Giuseppe Cappelletti

Cite This: https://doi.org/10.1021/acsami.4c05478 Read Online

ACCESS | Metrics & More | Article Recommendations | SI Supporting Information

ABSTRACT: Herein, the integration of SnO_2 nanoparticles with two Zn(II) porphyrins—Zn(II) 5,10,15,20-tetraphenylporphyrin (ZnTPP) and its perfluorinated counterpart, Zn(II) 5,10,15,20-tetrakis(pentafluorophenyl)porphyrin ($ZnTPPF_{20}$)—was investigated for the sensing of gaseous acetone at 120 °C, adopting three Zn-porphyrin/SnO_2 weight ratios (1:4, 1:32, and 1:64). For the first time, we were able to provide evidence of the correlation between the materials' conductivity and these nanocomposites' sensing performances, obtaining optimal results with a 1:32 ratio for $ZnTPPF_{20}/SnO_2$ and showcasing a remarkable detection limit of 200 ppb together with a boosted sensing signal with respect to bare SnO_2. To delve deeper, the combination of experimental data with density functional theory calculations unveiled an electron-donating behavior of both porphyrins when interacting with tin dioxide semiconductors, especially for the nonfluorinated one. The study suggested that the interplay between electrons injected, from the porphyrins' highest occupied molecular orbital to SnO_2 conduction band, and the latter's available electronic states has a dramatic impact to boost the chemiresistive sensing. Indeed, we highlighted that the key lies in preventing the full saturation of SnO_2 electronic states concomitantly increasing the materials' conductivity: in this respect, the best compromise turned out to be the perfluorinated porphyrin. A further corroboration of our findings was obtained by illuminating the sensors during measurements with light-emitting diode (LED) light. Actually, we demonstrated that it does not have any impact on improving the sensing behavior, most probably due to the electronic oversaturation and scattering caused by LED excitation in porphyrins. Lastly, the most effective hybrids (1:32 ratio) were physicochemically characterized, confirming the physisorption of the macrocycles onto the SnO_2 surface. In conclusion, herein, we underscore the feasibility of customizing the porphyrin chemistry and porphyrin-to-SnO_2 ratio to enhance the gaseous sensing of bare metal oxides, providing valuable insights for the engineering of highly performing light-free chemiresistors.

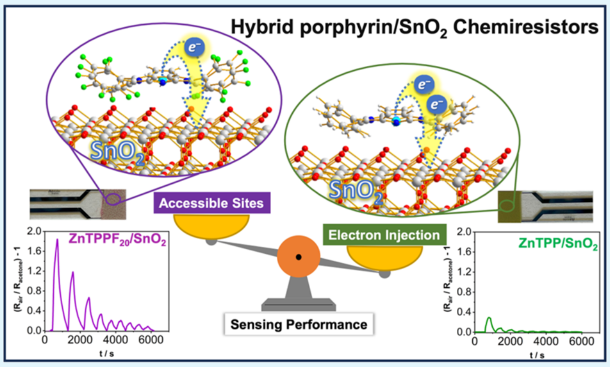

KEYWORDS: *chemiresistors, gaseous acetone sensing, tin dioxide, porphyrins, nanocomposites, density functional theory*

1. INTRODUCTION

In the realm of modern sensing technologies, chemiresistive gas sensing stands as a remarkable innovation that can play a critical role in detection of volatile organic compounds (VOCs) and toxic gases in various applications, ranging from environmental monitoring to industrial safety and medical diagnostics.[1−4] Delving deeper into the development of chemiresistive materials, i.e., mainly metal oxide semiconductors (MOS) as SnO_2, ZnO, and WO_3, both alone[5] or in combination in hybrid compounds,[6−8] cutting-edge advancements have been already done. In recent years, SnO_2, an n-type metal-oxide semiconductor with a band gap of 3.6 eV, emerged as a promising semiconductor for gas sensors.[9] However, the adoption of traditional SnO_2-based gas sensors continues to be limited by the inherent challenges shared by all MOS. In particular, cross-sensitivity (for which the sensor also responds to interfering species present in the environment), temperature dependency together with high operating temperature in the case of bare metal oxides, and humidity interference due to the MOS's high sensitivity to water vapor molecules are the primary causes of sensing worsening.[10−12] Therefore, to address some of these challenges, MOS have been usually combined with graphene oxide (GO),[13] reduced GO (rGO),[14] metal organic frameworks (MOFs),[15] and/or noble metal nanoparticles (as Au or Pd).[16,17]

In this context, porphyrins have emerged as highly promising materials in the field of chemiresistive gas sensors

Received: April 3, 2024
Revised: July 11, 2024
Accepted: July 15, 2024

based on MOS, particularly for the detection of VOCs. These cyclic organic compounds, characterized by a macrocyclic structure with an extended π-electron conjugation, thermal and chemical stabilities, quite good solubility, and high structural flexibility, have been investigated in a variety of different fields, such as catalysis,[18] optoelectronics,[19−21] third-generation photovoltaics,[22−25] and artificial photosynthesis.[26−28] Indeed, many reactive positions of the macrocycle (eight β-pyrrolic and four *meso* carbons, plus two axial positions in the presence of a central metal ion) allow a tailor-made synthesis and a fine-tuning of the electronic properties in view of a specific application,[29] including sensing.[30,31]

Actually, photoactive porphyrins exhibit remarkable versatility as ligand platforms, capable of both forming an extensive array of metal complexes and interacting with gaseous molecules through diverse mechanisms.[30] In fact, leveraging on their chemical versatility, porphyrins can be used to both enhance their hybridization with other compounds (as MOS) and tailor the sensing material's surface, so that the sensing performances may be improved.[32]

Given this backdrop, to the authors' best knowledge, very few research papers are focused on the combination of MOS with porphyrin macrocycles for sensing application, and most of them are focused on the use of zinc oxide as MOS.[31−37] Furthermore, to date, the only exploration of hybrid materials comprising porphyrins and SnO_2 demonstrates that this combination enhances the performance of optical oxygen sensors[38] and presents encouraging prospects for developing chemiresistive sensor materials capable of detecting mixed BTEX compounds.[39]

Generally, in a gas sensor employing chemiresistive technology with MOS functionalized by porphyrins, detecting electron donor species results in an augmented current and, consequently, in a reduction in resistivity, irrespective of the specific sensing mechanism. The most accredited model relies on resistance changes triggered by variations in the density of charge carriers, resulting from oxygen adsorption or desorption and formation of oxygen ions on the surface (i.e., ionosorption model).[10] Upon exposure to the target gas, its molecules react with the adsorbed oxygen anions, releasing trapped electrons back into the MOS conduction band, thus reducing sensor's resistance.[40] This resistance change is converted into an electrical signal, facilitating gas detection. Therefore, the conductivity of the metal oxide is mainly dependent on the density of oxygen ions adsorbed on the surface. In addition to that, so far published literature about sensing mechanisms of ZnO/porphyrin systems[32−34] primarily centers around the direct interaction between the organic macrocycles and the target VOC, offering electrons for injection into the MOS conduction band or regenerating the porphyrin cation formed postelectron transfer.[35] Albeit this interaction is commonly ascribed to the reversible adsorption and desorption processes taking place on the sensor's surface, there is no general consensus; thus, the precise role of porphyrins remains unclear and necessitates further elucidation. In any case, the outcome is an increase of the semiconductor's conductivity, which is related to the final response signal.

Therefore, in this study, we focus on the electronic effects arising from the intimate combination of n-type SnO_2 with porphyrins, featuring different electron-donating characters. Additionally, we consider various porphyrin-to-MOS weight ratios, aiming at roughing out a comprehensive overview of the system to understand the specific role played by the two materials. This approach yields valuable insights from both empirical and theoretical perspectives. In particular, Zn(II) 5,10,15,20-tetraphenylporphyrin (ZnTPP) and the perfluorinated counterpart Zn(II) 5,10,15,20-tetrakis(pentafluorophenyl)porphyrin ($ZnTPPF_{20}$) were chosen due to their peculiar electronic properties. Indeed, if, on the one hand, plain aryl groups in the *meso* position impart an electron-rich character to ZnTPP, on the other hand, the presence of multiple fluorine atoms in the perfluorinated counterpart ($ZnTPPF_{20}$) creates an electron-poor core, allowing us to investigate the possible impact of the porphyrin's electronic features on the final sensing. For both nanocomposites, we investigated three different Zn-porphyrin/SnO_2 ratios (namely, 1:4, 1:32, and 1:64) to assess the optimal one in terms of sensing properties toward acetone molecules at low−medium operating temperature (i.e., <150 °C). Acetone was chosen as the target analyte, being considered as the gaseous biomarker of diabetes type 1, and tin dioxide has proven to be more promising than zinc oxide according to authors' previous works.[41,42] Furthermore, since it has been stated that light can favor the sensing,[43] to finalize the investigation, its role was also studied by illuminating the samples during measurements. Lastly, ab initio calculations through density functional theory (DFT) were performed to possibly shed light on the porphyrins' role in the sensing mechanism of the synthesized nanocomposites.

2. MATERIALS AND METHODS

All of the chemicals were of reagent-grade purity and purchased from Merck; doubly distilled water passed through a Milli-Q apparatus was used. Free-base 5,10,15,20-tetraphenylporphyrin was purchased from Merck, whereas free-base 5,10,15,20-tetrakis(pentafluorophenyl)porphyrin was from PorphyChem Sas.

2.1. Synthesis of Pristine and Composite Materials.

Tin dioxide nanoparticles were synthesized as reported elsewhere.[13,42]

ZnTPP and $ZnTPPF_{20}$ were prepared according to the literature.[21,28] Briefly, the commercially available free-base TPP and $TPPF_{20}$ underwent a complexation reaction by refluxing the proper solution of porphyrins for 3 h ($CHCl_3$ for TPP and CH_3OH for $TPPF_{20}$) after addition of an excess of $Zn(OAc)_2$ in CH_3OH. The zinc complexes were purely obtained by evaporating the solvents from reaction mixtures and by washing and filtering the resulting powder from methanol (ZnTPP) or deionized water ($ZnTPPF_{20}$).

Once the materials, namely, SnO_2 and the two Zn-tetraphenyl porphyrins, were prepared, nanocomposites were fabricated by a simple dissolution/deposition method. The appropriate quantity of ZnTPP or $ZnTPPF_{20}$ was separately dissolved in 2 mL of CH_2Cl_2 and the specific amount of SnO_2 (to have 1:4, 1:32, and 1:64 porphyrin/metal oxide weight ratios) was dispersed in such solutions. The obtained mixtures were vigorously stirred for 3 h at room temperature. Then, the solvent was removed by means of a rotary evaporator under atmospheric pressure at 50 °C. The composites were subsequently collected and kept under vacuum overnight to fully remove solvent residues.

2.2. Material Characterizations and Sensing.

X-ray powder diffraction (XRPD) analyses were carried out on a Miniflex 600 Bragg−Brentano Bragg goniometer. We employed graphite-monochromated Cu Kα radiation (Cu $K_{\alpha 1}$ $\lambda = 1.54056$ Å, $K_{\alpha 2}$ $\lambda = 1.54433$ Å) at 40 kV × 40 mA nominal X-ray power. Diffraction patterns were collected between 10 and 80° with a step size of 0.02° and a total counting time of about 1 h. A microcrystalline Si-powdered sample was used as a reference to correct the instrumental line broadening effects.

The powders' morphology and surface structure were studied by scanning electron microscopy (SEM) performed on an SEM Leo 438 VP Zeiss instrument after their gold plating by means of a sputtering technique (Sputter Nanotech, Assing Instruments). High-resolution

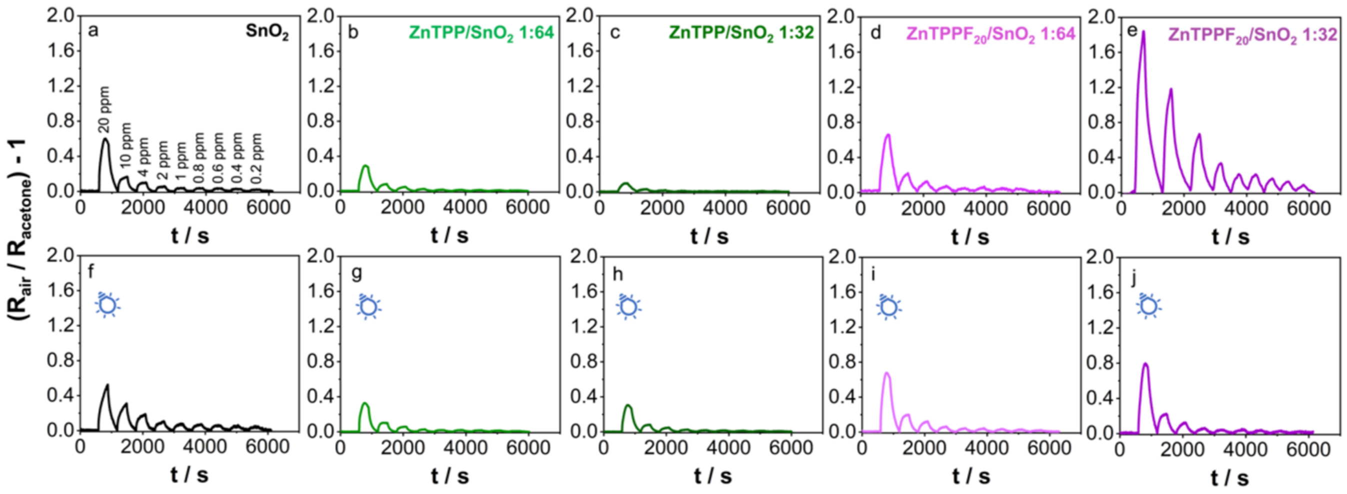

Figure 1. Sensors' responses toward acetone gaseous molecules (from 20 to 0.2 ppm) both without (upper row) and with (lower row) LED light. Tests were performed under simulated air (80% N_2−20% O_2) at an operating temperature OT = (120 ± 2) °C and relative humidity RH% < 2%.

transmission electron microscopy (HRTEM) analyses were performed on an FEI TECNAI G2 F20 instrument, operating at an accelerating voltage of 200 kV, equipped with an S-Twin lens that gives a point resolution of 0.24 nm. The TEM grids were prepared by dropping the dispersed suspension of nanoparticles in ethanol onto a holey-carbon-supported copper grid and drying it in air at room temperature.

The specific surface area and porosity were determined by a multipoint Brunauer−Emmett−Teller (BET) method using N_2 adsorption/desorption isotherms at 77 K using a Tristar II 3020 (Micromeritics) apparatus. Desorption isotherms were used to determine the total pore volume by using the Barrett−Joyner−Halenda (BJH) method. During the measurement, sample powders were thermally treated at 80 °C overnight to avoid any possible material degradation.

Attenuated total reflectance (ATR)-Fourier transform infrared reflectance (FTIR) spectra were acquired on a PerkinElmer Frontier instrument equipped with an ATR accessory with a diamond/ZnSe crystal. The IR spectra were registered between 4000 and 400 cm^{-1}.

ZnTPP and $ZnTPPF_{20}$ were characterized by ^1H- and ^{19}F-NMR, ultraviolet−visible (UV−vis) absorption spectroscopy, and thermogravimetric analysis. NMR spectra were acquired on a Bruker Avance DRX-400 instrument in $CDCl_3$ (Sigma-Aldrich). UV−vis electronic absorption spectra were recorded at room temperature in CH_2Cl_2, using a Shimadzu UV-3600 spectrophotometer and quartz cuvettes with a 1 cm optical path length. Thermogravimetric analysis (TGA) analysis was performed on a TGA 7 PerkinElmer instrument, connected to a TAC 7/DX interface and a gas selector to choose between air and nitrogen. The analysis was conducted in air, with a heating rate of 20 °C/min, ranging from 30 to 800 °C.

The nanocomposites were characterized by diffuse reflectance spectroscopy (DRS), using a double beam UV−vis−NIR scanning spectrophotometer (Shimadzu UV-3600 plus, Tokyo, Japan) equipped with a diffuse reflectance accessory (integrating sphere from BIS-603). The spectra were recorded in the wavelength range of 220−2600 nm. The finely ground powder sample was uniformly pressed in a circular disk (with an external diameter of 0.2 cm) included in the sample holder; the latter was inserted in a special quartz cuvette and fixed on a window of the integrating sphere for the reflectance measurements. $BaSO_4$ was the reflectance reference compound.

Nanocomposites were deposited by a hot-spray method on glass interdigitated platinum electrodes (Pt-IDEs, purchased from Metrohm and schematically depicted in Figure S1a) and sensing tests were carried out using a custom-built stainless-steel cell (see Figure S1b), as deeply described in authors' previous works.[44,45] In particular, the layer's resistance was measured while flowing a simulated air (80% N_2−20% O_2) gas mixture (with a total flow rate of 0.5 L min^{-1}) in the presence of different concentrations of acetone gaseous molecules. The flow of the target analyte was varied by dilution from a starting 500 ppm concentration (in a N_2 gas mixture) by Bronkhorst flow meters while keeping the total flow rate constant. The dynamic response (schematically displayed in Figure S1c) was recorded by an Autolab PGStat30 (Eco Chemie, Utrecht, The Netherlands) potentiostat/galvanostat controlled by NOVA 2.0 software, applying a constant bias of +1.0 V. The sensor signal is reported as $(R_{air}/R_{acetone}) - 1$, where R_{air} and $R_{acetone}$ are, respectively, the layer's resistances in simulated air and in the presence of acetone molecules, together with the relative response and recovery times according to the previous literature.[44,45] These last two parameters refer to the time needed to reach 90% of the response at a given VOC concentration and the corresponding time necessary to lose 90% of the signal. All of the tests were performed at a relative humidity lower than 2% (checked by inserting a hygrometer in the tube coming out from the sensing chamber) and at (120 ± 2) °C, and for some of them, light-emitting diode (LED) (THORLABS, at a wavelength of 455 nm, power of 2 W) and UV (Jelosil HG500 iron halide mercury arc lamp 500 W, emitting in the 350−450 nm range with an incident power density of 30 mW cm^{-2}) irradiation sources were also adopted.

To better investigate the electrical properties of the sensors, $I-V$ curves were recorded by varying the applied potential in the range −2/+2 V and measuring the current by means of an Autolab PGStat30 (Eco Chemie, Utrecht, The Netherlands) potentiostat/galvanostat controlled by NOVA 2.0 software.

2.3. Computational Details.

Ab initio calculations on the tetragonal rutile structure of SnO_2[46,47] were performed using DFT as implemented in the SIESTA code,[48] choosing PBE[49] as the exchange−correlation functional. Norm-conserving pseudopotentials for Sn and O were generated based on the Troullier−Martins parametrization.[50] The basis set for both atoms is of the DZP type with standard parameters. Bulk-phase calculations were performed on a 22 × 10 × 7 k-point grid in a 12 atom tetragonal unit cell, using a 450 Ry as mesh cutoff. A suitable cell of SnO_2 for a reliable description of the adsorption of ZnTPP/$ZnTPPF_{20}$ has been chosen as a 6 × 3 (110) surface unit cell and 2 trilayers in the direction perpendicular to the surface. This choice corresponds to mass ratios between the adsorbed porphyrins and the SnO_2 slab equal to 1/16 and ∼1/10 for ZnTPP/SnO_2 and $ZnTPPF_{20}$/SnO_2, respectively. The vacuum amount was 10 Å. The two-dimensional (2D) periodic system was thus composed of 72 Sn atoms and 144 O atoms. The Brillouin zone sampling was 4 × 4 × 1 k-points.

In order to overcome the heavy band gap underestimation typical of pure functionals, such as PBE, if necessary, we applied the half-occupation technique to the oxygen pseudopotential as described by

Table 1. Materials' Current Values in the Absence (i_{baseline}) and Presence (i_{acetone}) of Acetone Molecules and Response Intensity Reported as ($R_{\text{air}}/R_{\text{acetone}}$) − 1 Relative to the Signal at 20 ppm, Both with and without LED Light[a]

	LED off			LED on		
material	i_{baseline} (μA)	i_{acetone} (μA)	($R_{\text{air}}/R_{\text{acetone}}$) − 1, response intensity at 20 ppm	i_{baseline} (μA)	($R_{\text{air}}/R_{\text{acetone}}$) − 1, response intensity at 20 ppm	charge transfer
SnO_2	3	5	0.60	9	0.55	
ZnTPP/SnO_2 1:64	38	49	0.29	50	0.33	0.69
ZnTPP/SnO_2 1:32	64	70	0.10	53	0.30	1.36
ZnTPP/SnO_2 1:4	1700	n.d.	n.d.	1700	n.d.	4.32
$ZnTPPF_{20}/SnO_2$ 1:64	5	9	0.70	8	0.72	0.25
$ZnTPPF_{20}/SnO_2$ 1:32	20	56	1.80	10	0.80	0.45
$ZnTPPF_{20}/SnO_2$ 1:4	610	n.d.	n.d.	620	n.d.	1.97

[a] The charge transfer has been estimated computationally considering the electrons donated from porphyrins to 100 SnO_2 formula units.

Ferreira et al.,[51,52] which led to great improvements in the band gap value. After the treatment, the latter increased from 0.74 to 3.20 eV, which is much closer to the experimental gap of 3.60 eV reported in the literature.[47]

3. RESULTS AND DISCUSSION

3.1. Acetone Sensing. First, to guarantee that the direct current measurements accurately reflect the conditions at the oxide−electrode interface without being influenced by any possible potential barrier, *I*−*V* curves were collected for SnO_2, ZnTPP/SnO_2 1:32, and $ZnTPPF_{20}/SnO_2$ 1:32 modified IDEs (as representative ones). As clearly visible in Figure S2, all of the materials showed a linear trend that perfectly matches the first Ohm's law, thus indicating a good electrical contact between the sensing layer and the electrode's material.[53]

Then, to investigate the sensing properties of the prepared nanocomposites, gaseous acetone was chosen as the target analyte. Figure 1 shows the obtained results after purging different acetone concentrations (from 20 ppm down to 200 ppb) both without and with the aid of LED light at a constant operating temperature of 120 °C and very low relative humidity (RH% below 2%). Focusing first on outcomes in dark conditions, it is striking to see that the two porphyrins have a different impact on the sensing when combined with SnO_2. In both cases, the highest porphyrin/SnO_2 weight ratio of 1:4 did not result in any appreciable response upon purging the target VOC, as well as porphyrins alone did not show any perceptible sensing behavior (as depicted in Figure S3 for $ZnTPPF_{20}$).

Delving into specifics, it seems that the two ZnTPP-based nanocomposites (namely, 1:64 and 1:32 ratios; Figure 1b,1c) do even worsen the sensing behavior of the pristine SnO_2, especially increasing the amount of the porphyrin in the nanocomposite. Conversely, the presence of $ZnTPPF_{20}$ influences the MOS performances in a completely different way, especially in the case of the 1:32 sample, which exhibited sharper and higher sensing responses with respect to those of bare SnO_2 (Figure 1a,1d,1e and Table 1, fourth column). This sample gave an outstandingly 3 times greater signal at a given concentration of 20 ppm, and in general, higher sensing signals were recorded for all of the investigated acetone amounts down to 200 ppb. To elucidate these significant differences among nanocomposites and diverse ratios, we thoroughly examined the electrodes' currents in simulated air (called baseline current from now onward), after having stabilized the systems and before purging acetone molecules inside the sensing chamber. An overview of the acquired data is reported in Table 1 (2nd column). Generally, the presence of both porphyrins leads to an increase of the current value with respect to bare SnO_2 even if, mainly in the case of ZnTPP, this rise is more prominent and the current predictably becomes greater and greater by adding more porphyrin in the composites. Analogously, a similar tendency was noticed for the $ZnTPPF_{20}$-based samples with the exception that the absolute values are lower than the corresponding ones of ZnTPP (Table 1, second column), as expected by the higher molar mass of $ZnTPPF_{20}$ with respect to ZnTPP and to the lower tendency of the former to transfer electrons, as shown by theoretical estimates (Table 1, seventh column). As such, considering that the final response is a ratio between the compounds' resistances in air and in the presence of the target VOC (i.e., ($R_{\text{air}}/R_{\text{acetone}}$) − 1), we can infer that, if the adsorption of porphyrins onto SnO_2 leads to a moderate increase of sensors' conductivity (in air, as, for instance, from 3 μA of bare SnO_2 up to 20 μA in the case of $ZnTPPF_{20}/SnO_2$ 1:32), this rise will boost the final chemiresistive performances. Contrarily, when the sensing materials produce an excessive increase of the baseline current, as in the case of a high porphyrin/SnO_2 ratio and/or by using stronger donor porphyrins (i.e., ZnTPP), a decline of performances will be observed.

Besides, a remarkably different behavior was seen when LED illumination illuminated the electrodes during the entire sensing measurement. Pristine SnO_2 displayed no significant rise in its baseline current (Table 1, fifth column) since LED fixed wavelength does not fall into SnO_2 band gap (around 3.60 eV),[42] therefore not guaranteeing the electrons' promotion from the valence band to the conduction one, and subsequently an increase of the system's conductivity. Likewise, in the case of ZnTPP-based nanocomposites (Figure 1g,h), no noteworthy observations can be made and the recorded trend of both baseline currents (Table 1, fifth column) and signals' intensities (Table 1, sixth column) roughly resembles the one in dark conditions. Conversely, the situation is somewhat different in the case of $ZnTPPF_{20}$-based composites (Figure 1i,1j): LED light seems to worsen the behavior of 1:32 ratio, resulting in a signal's decrease from 1.80 to 0.80. It is conceivable that the light source influences porphyrins' electronic behavior rather than the tin dioxide one. Therefore, considering the former's attitude to increase the nanocomposites' overall conductivity, further electronic excitation of the macrocycles might be detrimental. We assume, indeed, a greater electron injection from porphyrins to SnO_2 upon illumination, with a subsequent rise in electrons scattering inside the material.[54,55] This phenomenon characterized by a larger electronic dispersion might lead to a more

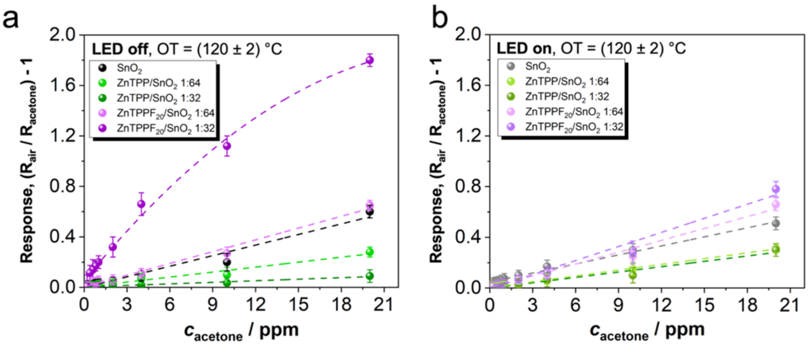

Figure 2. Comparison of signal responses versus different acetone concentrations both (a) without and (b) with LED illumination. OT = operating temperature.

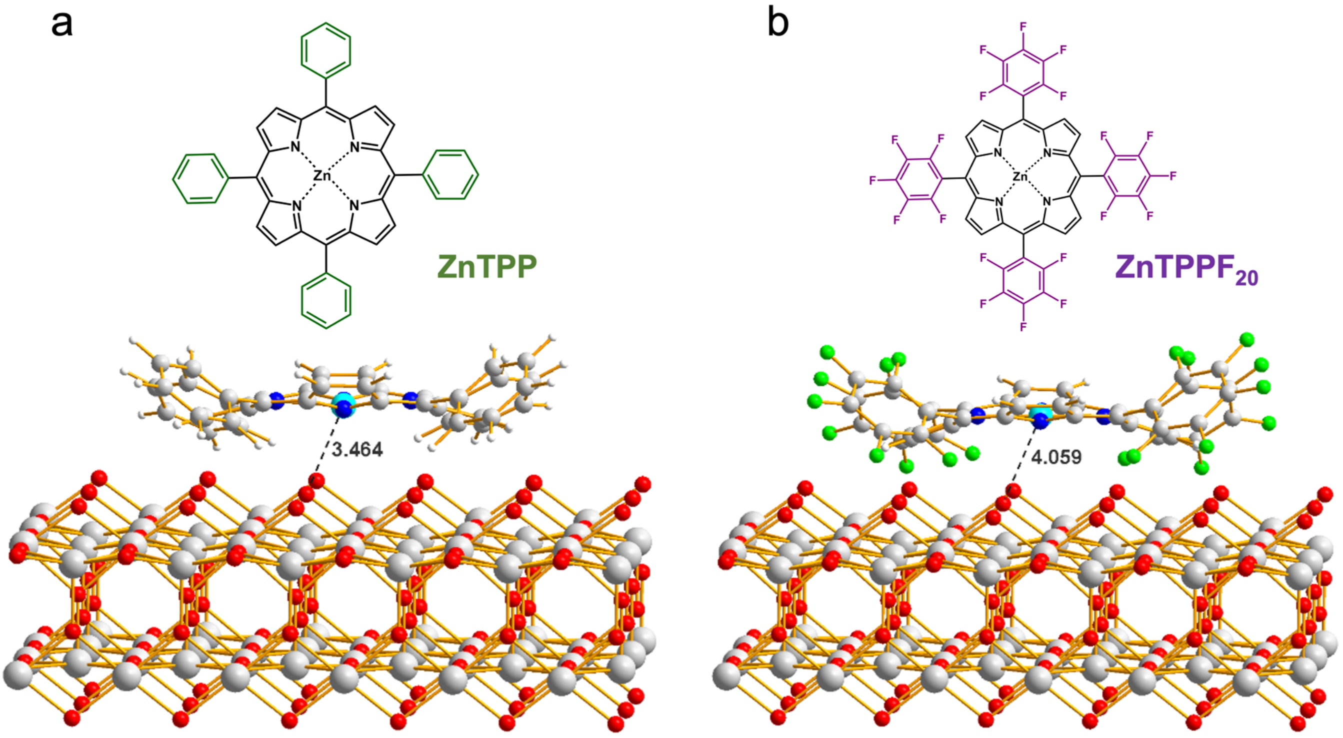

Figure 3. Ab initio optimized structures of the (a) ZnTPP/SnO$_2$ and (b) ZnTPPF$_{20}$/SnO$_2$ nanocomposites together with the relative chemical structure. The shortest Zn−O distances (in Å) are shown as dashed lines.

disordered system and, thus, to its conductivity decrease (baseline current around 10 μA; Table 1, sixth column) and, ultimately, to a worsen sensing (halved signal's intensity). To have a better understanding of the whole system, measurements under UV illumination were also carried out (Figure S4). As expected, the lower light wavelength can be beneficial only in the case of pristine oxide, causing an increase in the signal's intensity. On the contrary, the presence of porphyrin molecules, adsorbed onto the SnO$_2$ surface (see HRTEM images in the following), seems to interfere, and UV light does not appear to be of any help for sensing. As such, we can infer that our ZnTPPF$_{20}$/SnO$_2$ 1:32 nanocomposite has promising applicability in hand-held sensors, owing to its ability to give an optimal signal even without the aid of a light source.

Furthermore, plotting the responses as a function of the purged acetone concentrations, a linear fashion is well-visible for all of the tested compounds, both in the dark and under LED light, with the only exception being the ZnTPPF$_{20}$/SnO$_2$ 1:32 composite (LED off), for which a change in trend is clearly observable by increasing the VOC amount (Figure 2, second-degree function reported as dashed violet line). Indeed, notwithstanding a lower slope can be easily and reasonably seen after 4 ppm, no plateau region is reached until 20 ppm and so the system—in this concentration range—does not show any Langmuir-like behavior, which results in agreement with the available literature.[56] This singular behavior might be ascribable to a partial degree of active sites' saturation and/or consumption/reduced accessibility of the negatively charged adsorbed oxygen species with the increase of acetone concentration.

In addition, alongside signal's intensity, two other parameters need to be considered to define the performances of a chemiresistor, i.e., the response and recovery times. Herein, all of the investigated compounds showed roughly similar values with an average response time of about 120−150 s and a recovery one of around 200−220 s. Considering that literature about porphyrin/SnO$_2$ coupling for acetone detection is basically nil, a comparison between our

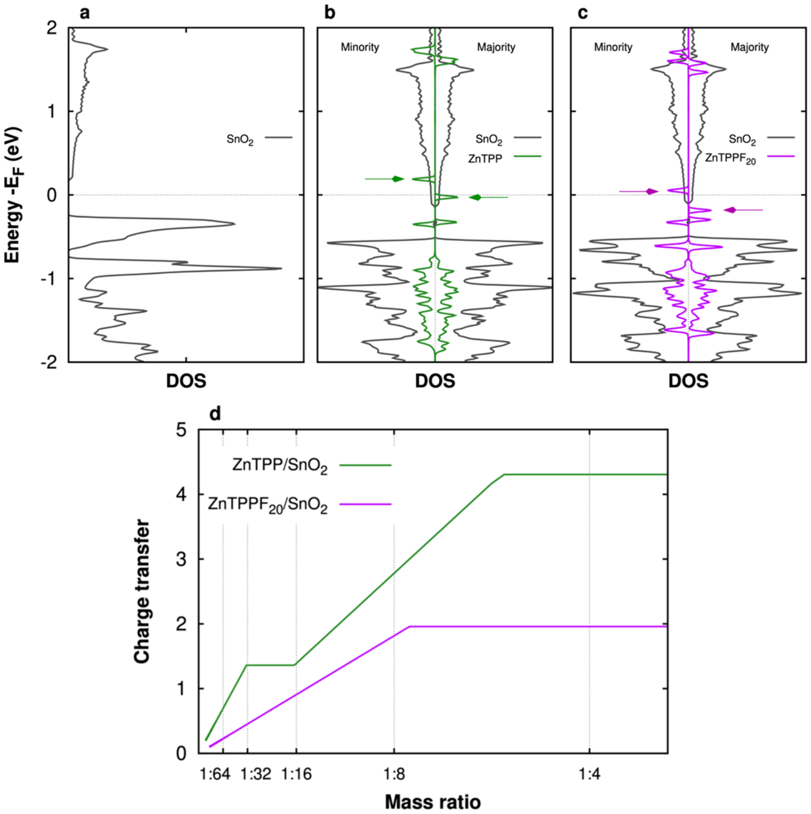

Figure 4. Spin-resolved density of states (DOS) of (a) pristine $SnO_2(110)$, (b) ZnTPP, and (c) $ZnTPPF_{20}$ adsorbed on the SnO_2 surface. Green and violet lines refer to the molecular contribution to the total DOS, whereas the original HOMO spin components are indicated by green and violet arrows. (d) Charge transfer as a function of the mass ratio porphyrin/MOS, estimated considering the electrons donated from ZnTPP/$ZnTPPF_{20}$ to 100 SnO_2 formula units.

response/recovery times with those already published, obtained with the same material systems and gas environments, is barely possible. However, on the basis of the most recent studies,[57,58] we can assume that our sensors' performances are in line with the already reported highly efficient chemiresistors for acetone sensing operating at low temperatures.

3.2. Sensing Mechanism: The Role of Porphyrins.

Trying to unveil the possible sensing mechanism and especially the singular electronic properties of the synthesized nanocomposites, ab initio calculations on the Zn(II) porphyrin-based adducts were carried out using DFT. Both the SnO_2 bulk and (110) surface, which is reported to be the most stable one,[59−61] were simulated and, once verified through the comparison with recent literature[59] that our computational setup gave reliable results, we devoted our attention to the structures of the two $ZnTPP/SnO_2$ and $ZnTPPF_{20}/SnO_2$ hybrids. In our calculations, the coordinates of the oxygen atoms of the MOS upper layer and of all of the atoms of the porphyrin molecules were optimized to take into account both surface relaxation effects and the distortion of the porphyrin's conformation with respect to the gas phase due to the interaction with the solid substrate. The electron density distribution of the systems was analyzed within the framework of the Quantum Theory of Atoms in Molecules (QTAIM)[62] using the Critic2 code.[63] Due to the limited number of atoms that can be treated ab initio, we considered a MOS surface sample with a reduced thickness of only 2 trilayers (see Figure 3) and a planar adsorption of the porphyrins' molecules onto the SnO_2 surface. We are aware that porphyrins can lay down in different ways on the semiconductor substrate,[64,65] depending on both the rotation angle of the porphyrin core and the Zn position with respect to the SnO_2 lattice. However, the nature of the interaction between the macrocycles and the substrate (SnO_2) is mainly a weak electrostatic atom−atom interaction between the large, highly symmetric, highly conjugated, apolar adsorbed molecules and a periodic SnO_2 lattice with regular alternation of negative (O) and positive (Sn) ions extending all over the surface. Therefore, regardless of the mutual orientation of the macrocycles with respect to the substrate, the atoms in close contact are the same, resulting in a global intermolecular interaction energy having the same strength and nature. This means that, aiming at deriving a reliable estimate of the porphyrin-to-MOS charge transfer, which causes an overall materials' current increase, the role of the adsorption configuration can be considered negligible.

For both nanocomposites, the most stable solution turned out to be magnetic, its energy being lower by 0.2 eV than the value obtained through a nonmagnetic calculation. The computed adsorption energies were equal to 3.55 and 4.12 eV for ZnTPP and $ZnTPPF_{20}$, respectively: these values reflect the large overlapping area between the substrate and the adsorbed molecules and are consistent with the nature of the intermolecular interactions, resulting in a significant charge transfer from the macrocycles to the MOS surface. For this topic, we have found that ZnTPP donates 1.23 e^-, whereas $ZnTPPF_{20}$ gives only 0.78 e^-, in agreement with their electronic properties. Indeed, looking at the spin-resolved density of states (DOS) graphs (Figure 4), two fundamental remarks can be highlighted: first, for $ZnTPP/SnO_2$, a sharp

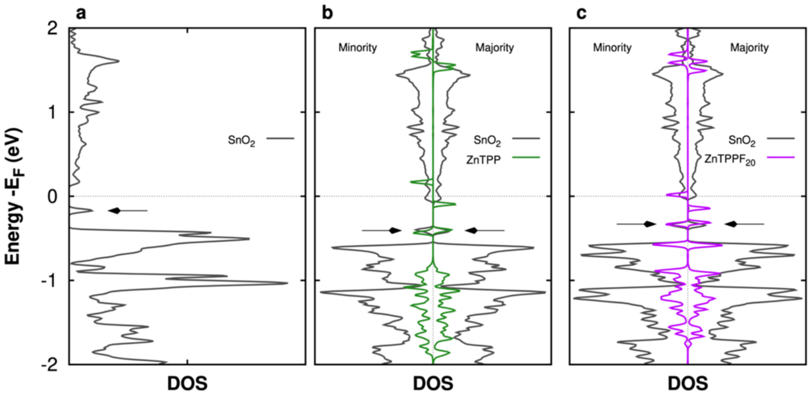

Figure 5. Spin-resolved density of states (DOS) of (a) $SnO_2(110)$ defective surface, (b) ZnTPP adsorbed on the defective $SnO_2(110)$ surface, and (c) $ZnTPPF_{20}$ adsorbed on the defective $SnO_2(110)$ surface. Green and violet lines refer to the molecular contribution to the total DOS. Black arrows refer to defect states.

peak of the minority spin component of the original highest occupied molecular orbital (HOMO) (green arrow in Figure 4b, left side) is located above the Fermi level (thus being empty), whereas the peak of the HOMO majority spin component (green arrow in Figure 4b, right side) is pinned at the Fermi level (thus being partially empty). This result is in agreement with the number of transferred electrons (i.e., 1.23 e^-) and with a partial filling of the SnO_2 conduction band (CB) due to its superposition with the frontier molecular orbital of ZnTPP. Second, for $ZnTPPF_{20}/SnO_2$, the peak of the minority spin component (violet arrow in Figure 4c, left side) is partially empty, while the majority spin component peak of the original HOMO (violet arrow in Figure 4c, right side) is located below the Fermi level and is therefore filled. These findings explain the lower charge transfer (0.78 e^-) with respect to the $ZnTPP/SnO_2$ system. In other words, ZnTPP is more prone to give electrons to the SnO_2 surface rather than the $ZnTPPF_{20}$ molecule, in agreement with the presence of electron-withdrawing fluorine atoms.

Extending further the investigation from a theoretical point of view, the charge transfer from Zn(II) porphyrins to the SnO_2 substrate has been correlated to the experimentally explored porphyrin-to-SnO_2 weight ratios (Table 1, seventh column; Figures 4d and S5 together with the description of the charge transfer estimation). In Figure 4d, the estimated charge transfer as a function of the weight ratio has been drawn, starting from the energy positions of the partially occupied HOMO state with respect to the bottom of the MOS CB. Details of this procedure are reported in the Supporting Information. It is plainly evident that in the case of $ZnTPP/SnO_2$, at the same level of mass ratio, more electrons are given to tin dioxide with respect to $ZnTPPF_{20}/SnO_2$, therefore corroborating the so far reported speculations.

Eventually, we considered a defective metal oxide, i.e., with a surface oxygen vacancy: in this case, two extra electrons are released into the system and, according to our QTAIM calculations, for both $ZnTPP/SnO_2$ and $ZnTPPF_{20}/SnO_2$, the charge transfer is reduced by 0.2 electrons (with respect to the previously mentioned results), amounting to 0.55 e^- and to 1.03 e^- for fluorinated and nonfluorinated porphyrins, respectively. This scenario is confirmed by the DOS data shown in Figure 5. It is observable that, at an energy of about −0.32 eV below the CB, there is a pair (spin up and spin down) of states in the gap belonging to the substrate (black arrows). This suggests that the defect states containing the two extra electrons, made available by the presence of the vacancy, are spatially localized, and therefore, they do not participate in the conduction. For the sake of clarity, the DOS of the clean surface (with vacancy) is shown in the left panel of Figure 5: it confirms that the defect state is sharp and localized in the band gap (black arrow).

Combining experimental findings with theoretical calculations, a series of deductions can be drawn. Empirically, we noticed that the coupling of SnO_2 with ZnTPP is somewhat detrimental to the acetone sensing properties, whereas the $ZnTPPF_{20}$-based nanocomposites displayed a boosted signal with respect to pure SnO_2, especially without the aid of light (Table 1, fourth column). Theoretical analysis, on the other hand, revealed that ZnTPP is more inclined to bestow electrons upon physisorption onto the SnO_2 surface. These considerations suggest that a high injection of electrons in the conduction band of the MOS is not always beneficial for the gas sensing properties. The key point is that electrons are injected from the porphyrins' HOMO to the conduction band of SnO_2, and the former will thereby be depleted of electrons. However, since the MOS-accessible states with an energy lower than the HOMO are limited, there could be a complete filling of all of them, consequently hindering further electronic transfer upon interaction with the chemiresistive material. To be specific, in this case, electron donation upon acetone interaction with SnO_2 would not occur, and although there might be an electronic injection to the empty porphyrins' HOMO, no variation of the sensor's resistance and, as a consequence, no signal would be observed since these orbitals do not contribute to the conduction.

Herein, the HOMO of ZnTPP is higher in energy with respect to the one of $ZnTPPF_{20}$, so more states are potentially accessible, but at the same time, ZnTPP is also more prone to give electrons, as previously said. Hence, upon comprehensive consideration, it can be asserted that ZnTPP porphyrin may inject too many electrons into the MOS CB, thus saturating the accessible states and so preventing the response upon the interaction of the target analyte with the semiconductor. Conversely, the fluorinated porphyrin can prevent the complete filling of the accessible states, since it injects a lower number of electrons, thus preserving the final sensing signal. Moreover, the relative concentration between the porphyrin and the tin dioxide does play a pivotal role. When the porphyrins' concentration is reduced (i.e., 1:64 ratio), the number of accessible states in the MOS conduction band per

https://doi.org/10.1021/acsami.4c05478
ACS Appl. Mater. Interfaces XXXX, XXX, XXX−XXX

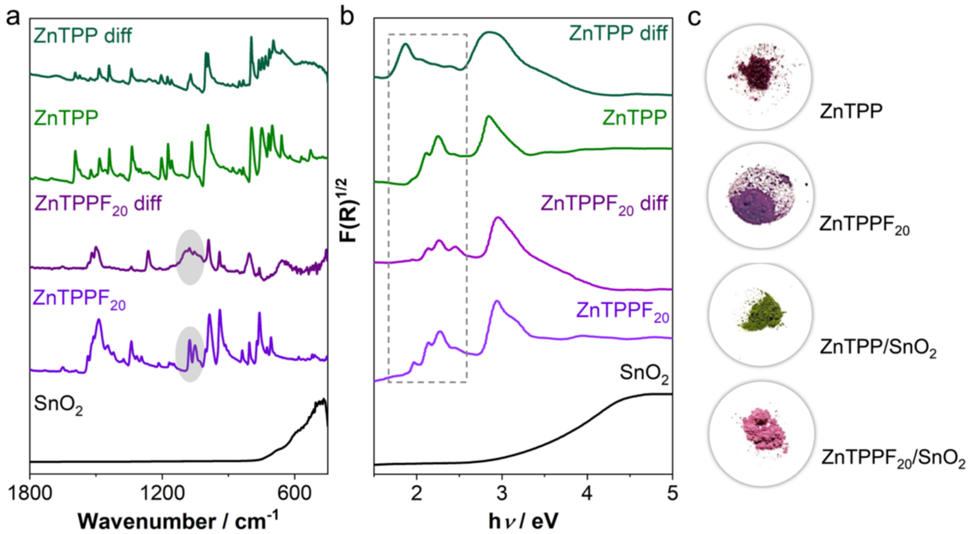

Figure 6. Comparison of (a) FTIR and (b) DRS spectra between those related to pristine porphyrins or SnO$_2$ and the corresponding ones obtained as a difference between porphyrin/SnO$_2$ 1:32 composites and bare SnO$_2$. Observable differences are highlighted in gray. (c) Comparison of pristine ZnTPP and ZnTPPF$_{20}$ with ZnTPP/SnO$_2$ and ZnTPPF$_{20}$/SnO$_2$ powders (1:32 ratio).

porphyrin molecule increases, and the other way round. This means that when the porphyrin concentration is too low, the electron pumping is insufficient to be beneficial for the sensing, whereas at a high porphyrin concentration (as 1:4), too many electrons are injected saturating all the accessible states, thus worsening the performances.

On top of this, as brought up earlier, in the literature, there is an open debate about the chemiresistive sensing mechanism: on the one hand, there is the so-called and widely embraced ionosorption model[10]—in which the detection of a reducing or oxidizing analyte is due to the variation of the negatively charged oxygen species ionosorbed onto MOS surface—on the other hand, the oxygen vacancy model—for which the target/MOS interaction is described by the partial reduction and reoxidation of the material's surface.[10] Concerning the former, it is widely believed that the oxidation of adsorbed acetone primarily contributes to the influx of additional electrons into the conduction band of the MOS, thereby augmenting the electronic currents. Specifically, in this model, the presence of charged oxygen species on the MOS surface plays a pivotal role,[10] participating in the acetone oxidation process, giving off their negative charge into the substrate. Thus, two distinct phases, each manifesting different electrical responses, can be recognized: first, the MOS surface with adsorbed charged oxygen species (no pumped acetone), and second, the same surface with fewer charged oxygen species (pumped acetone and its consequent oxidation/desorption).

With this reasoning in mind, we attempted to elucidate the present experimental findings from a theoretical point of view within the framework of the Drude model for conductivity, which states that conductivity is directly proportional to the number of charge carriers in the system. As previously outlined, the primary effect of porphyrin adsorption on the SnO$_2$ surface is the transfer of a negative charge from the porphyrin to the substrate. An approximate estimate of this charge transfer is provided in the last column of Table 1. A comparison with the measured current in the absence of acetone pumping (Table 1, third column) confirms that the greater the charge transfer, the higher the measured current.

Besides, the response to acetone adsorption (see also Table S1 and Figure S6) is somewhat more intricate, necessitating the consideration of multiple steps:

1. Presence of charged oxygen species. Our calculations (see Tables S2 and S3 and Figure S7) indicate that the additional electrons supplied to the MOS from the Zn-porphyrins lead to an increase in charged oxygen species on the surface, consistent with prior literature[59] and that this charge transfer is essentially independent from the exposed crystallographic plane. In our scenario, electrons are transferred by the added porphyrin, resulting in a higher charge density in the MOS and consequently, an increased presence of ions on the surface.
2. Oxidation of acetone. Upon interaction with the MOS surface, acetone undergoes oxidation. Any oxidation event involving charged oxygen species returns electronic population to the substrate (back-donation).
3. Effect of the mass ratio on the CB filling. Back-donated electrons may either augment or not the density of charge carriers, thereby influencing the measured current. Indeed, the lower empty states in the substrate may reside in the conduction band of the MOS or in localized states on porphyrins. In the latter case, the back-donated electrons will not contribute to the electronic current. This scenario could occur for specific values of the porphyrin/MOS mass ratio. Specifically, for ZnTPPF$_{20}$ and ZnTPP at a mass ratio of 1:32, the additional electrons back-donated by the oxygen anions participating in the oxidation events exhibit distinct behaviors: in the former case, they contribute to the charge carrier density, whereas in the latter, they do not (evidenced by a kink in the green line at a mass ratio of 1:32 in Figure 4d).

3.3. Physicochemical Characterizations of the 1:32 Porphyrin/SnO$_2$ Composites.

Both single materials (SnO$_2$ and porphyrins) and the most promising nanocomposites (i.e., 1:32 ratio) were finely characterized to investigate their possible interaction.

Regarding pristine SnO$_2$, the polymorph obtained through our proposed synthetic route is cassiterite, as clearly visible in

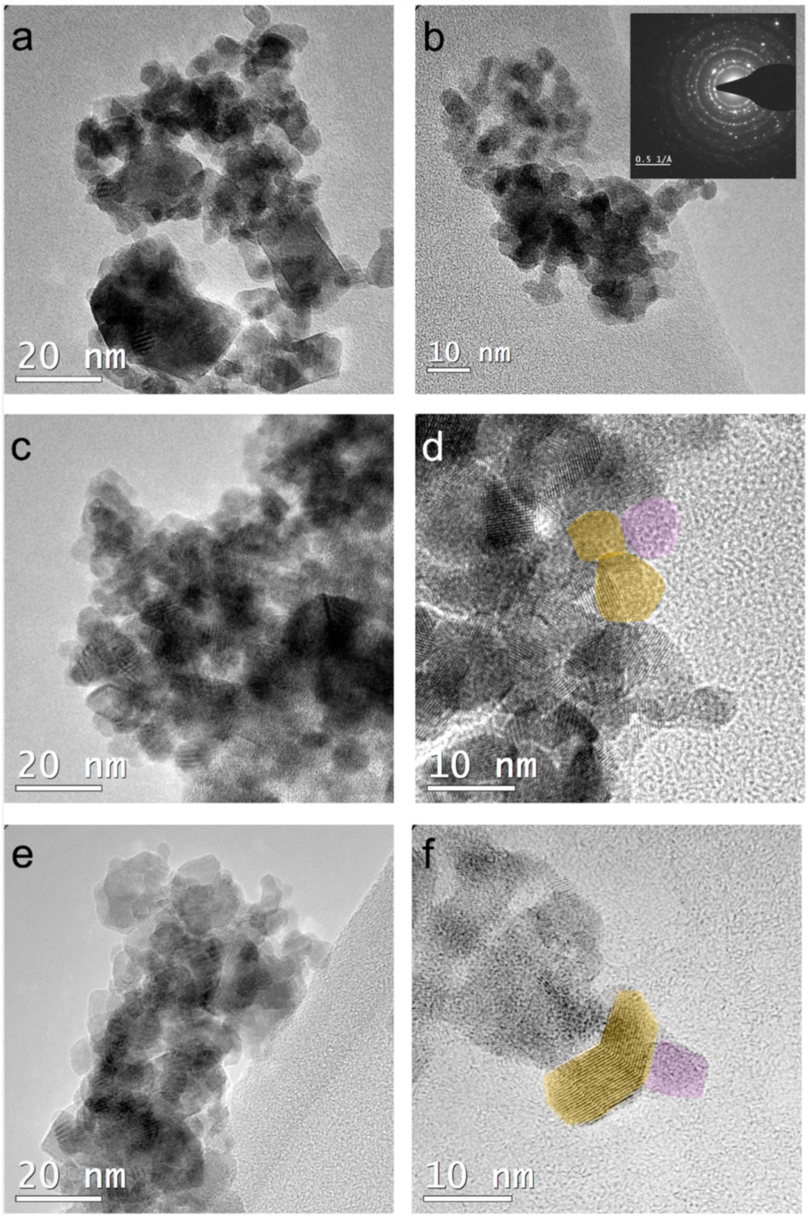

Figure 7. HRTEM images relative to (a, b) pristine SnO_2 (inset: selected area electron diffraction), (c, d) ZnTPP/SnO_2 1:32 and (e, f) ZnTPPF20/SnO_2 1:32 composites (crystalline SnO_2 and porphyrin/SnO_2 materials have been highlighted in yellow and pink, respectively).

Figure S8. Interestingly, there is no any appreciable change in the XRPD pattern when SnO_2 is coupled with the two adopted porphyrins: tin dioxide nanoparticles seem to retain their crystallinity and polymorphic structure. In addition, no new peaks appeared in the corresponding spectra.

On the other hand, UV–vis, ^{1}H-/^{19}F-NMR, and TGA analyses were performed to give an insight into porphyrins' chemical and structural properties (Figure S9). The UV/vis absorption spectra in CH_2Cl_2 show the typical pattern of porphyrin complexes predicted by the Gouterman's "four orbitals" model,[66] with an intense ($\varepsilon \approx 10^5$ M^{-1} cm^{-1}) Soret or B band in the range 400−420 nm, due to a $S_0 \rightarrow S_2$ transition, and two less pronounced ($\varepsilon \approx 10^4$ M^{-1} cm^{-1}) Q bands at 540−600 nm, given by $S_0 \rightarrow S_1$ transitions. All of the bands of $ZnTPPF_{20}$ show a sizable hypsochromic shift in comparison to those of ZnTPP as an effect of the presence of electron-withdrawing fluorine atoms. Also, NMR spectroscopy confirms the expected structures with a singlet for the *β*-pyrrolic protons of $ZnTPPF_{20}$ and a downfield shift in comparison to ZnTPP in the ^{1}H NMR spectrum, and three signals in the ^{19}F-NMR spectrum, due to the fluorine atoms in *ortho* (−136 ppm), *para* (−151 ppm), and *meta* (−161 ppm) positions of the pentafluorophenyl rings. Finally, TGA analysis confirms the stability of both ZnTPP and $ZnTPPF_{20}$ at the sensor operating temperature (120 ± 2) °C.

Insofar as it concerns the composites, the 1:32 ratio was chosen as the representative sample, having shown the optimal sensing behavior, especially in the case of $ZnTPPF_{20}$. Starting from structural features, FTIR data of the nanocomposites were elaborated by subtracting the spectrum of pure SnO_2 to isolate the contribution of only porphyrins (Figure 6a). Then, the obtained curves (labeled as difference spectra) were compared to those of the pure porphyrins to possibly spot any differences, peculiar to the SnO_2−porphyrin interaction. As displayed in Figure 6a, an appreciable variation in the bands of C−F stretching modes (at around 1000−1100 cm^{-1}, highlighted in gray) is clearly visible in the case of the ZnTPPF$_{20}$-based sample, evidencing a plausible interaction between the porphyrin and the MOS. On the contrary, for the other nanocomposite, no significant dissimilarities can be seen, probably due to the moderately weak planar physisorption of the organic macromolecules on the SnO$_2$ surface.

Besides, the 1:32 composites' optical properties were investigated by DRS, and the recorded spectra, after subtraction of the SnO$_2$ one, were compared to those of pure ZnTPP and ZnTPPF$_{20}$ powders (Figure 6b). The typical spectral pattern of Zn(II) porphyrins, previously observed in solution (Figure S9a), is also present in the DRS spectra of the pristine powders and remains clearly perceivable in the nanocomposites. As in solution, the presence of fluorine atoms produces a sizable 4−15 nm ipsochromic shift of all of the bands in the spectrum of ZnTPPF$_{20}$ in comparison to ZnTPP. Furthermore, the analysis of the differential DRS spectra confirms the interaction between the porphyrins and SnO$_2$.[67] Indeed, in perfect match with the colors, observable with the naked eye, for the pristine porphyrin complexes and the hybrids (Figure 6c), the differential spectrum of ZnTPP shows a marked enlargement of the Soret band and a significant alteration in the Q-band region (highlighted with a dashed gray line), with only one intense and red-shifted Q-band in comparison to the pristine powder. For ZnTPPF$_{20}$, on the other hand, even if the differential DRS spectrum and the powder spectrum are almost superimposable, a slight broadening and a small shift at higher energies (ca. 3 nm) of the Soret band are observable. Computationally speaking, we further corroborated this observation estimating a HOMO−lowest-unoccupied molecular orbital (LUMO) gap decrease of approximately 0.2 eV upon the adsorption of a ZnTPP molecule onto the SnO$_2$ surface. Lastly, in the case of bare SnO$_2$, it was possible to compute the band gap value of around 3.2 eV through the Kubelka−Munk elaboration, as reported elsewhere.[68]

Concerning the specific active surface area (S_{BET}) and the pores' volume distribution, the results are reported in Figure S10. The comparative histograms relative to the pores' distribution reveal for the two composites a trend very close to the tin dioxide's one, with the majority of pores centered in the range between 5 and 22 nm. Conversely, the surface area is slightly reduced (around 50 m^2 g^{-1}) when porphyrins are combined with SnO$_2$ (S_{BET} of 76 m^2 g^{-1}, see the inset of Figure S10), as expected. Indeed, the presence of the organic materials could lead to a partial covering effect and pore clogging of the MOS nanoparticles.

From a morphological point of view, SEM and HRTEM analyses were performed. From the former, it is well visible that the surface texture of the pristine oxide slightly modifies in the nanocomposites (Figure S11). Indeed, both ZnTPP/SnO$_2$ and ZnTPPF$_{20}$/SnO$_2$ 1:32 show a fluffier morphology, made of aggregates of around 2 μm, whereas bare tin dioxide is characterized by bigger agglomerates of tens of microns. Furthermore, direct evidence of porphyrins' presence comes from energy-dispersive X-ray spectroscopy results obtained in the case of the perfluorinated-based nanocomposite (Figure S11d). Actually, it was possible to detect a small peak ascribable to fluorine atoms, therefore corroborating the presence of the organic molecules. On the contrary, Zn(II) was not found in both the hybrids, which can be expected being the macrocycles' content very low (1:32) with respect to SnO$_2$. HRTEM images of pristine SnO$_2$ (Figure 7a,7b) show nanoparticles spherical in shape and with an average diameter of approximately 4 nm. In addition, the selected area electron diffraction (SAED) spectrum (inset of Figure 7b) reveals the characteristic electron diffraction pattern of SnO$_2$ cassiterite.[69] Interestingly, in the case of ZnTPP (Figure 7c,7d) and ZnTPPF$_{20}$-based nanocomposites (Figure 7e,7f), both crystalline and amorphous phases can be observed, which have been highlighted in yellow and pink color, respectively. In particular, portions of this amorphous phase, located around and among SnO$_2$ nanoparticles, might be ascribable to the porphyrin's adsorption leading to a local loss of the visible crystallinity. Conversely, MOS nanoparticles are clearly recognizable due to the evident crystalline planes.

Hence, from all of the obtained physicochemical results, we can conclude that we successfully managed to attain, through the adopted synthetic route, an intimate contact between the two macrocycles and tin dioxide nanoparticles.

4. CONCLUSIONS

In this work, we reported the integration of SnO$_2$ nanoparticles with Zn(II) 5,10,15,20-tetraphenylporphyrin (ZnTPP) and the perfluorinated counterpart Zn(II) 5,10,15,20-tetrakis-(pentafluorophenyl)porphyrin (ZnTPPF$_{20}$), i.e., two porphyrins characterized by peculiar electronic features. Three different Zn-porphyrin/SnO$_2$ weight ratios (namely, 1:4, 1:32, and 1:64) were chosen and adopted as active sensing materials for the low temperature (120 °C) detection of gaseous acetone molecules. We demonstrated the correlation between the materials' conductivity in air and their final sensing performances—in terms of signal's intensity—upon interaction with the target analyte. A too low (<20 μA) or a too high (>30 μA) hybrid's baseline current value seems, indeed, to be detrimental. As such, the ratio of 1:32 was the optimal one for both Zn-porphyrins, showing an outstanding performance with respect to pristine SnO$_2$, especially in the case of the ZnTPPF$_{20}$-based nanocomposite (with a detection limit of 200 ppb).

Moreover, by coupling the experimental findings with DFT calculations, we evidenced a distinctive electron-donating behavior exhibited by both macrocycles upon interacting with tin dioxide semiconductors and, as expected, this phenomenon was more pronounced in the case of the nonfluorinated one. Actually, if the MOS is electron-rich, acetone sensing may be highly hindered. Therefore, the perfluorinated porphyrin, donating a lower number of electrons than ZnTPP, may prevent the saturation of SnO$_2$ available electronic states, concomitantly increasing the nanocomposite's conductivity and, ultimately, allowing a better sensing. This result emerges also when considering computationally the semiconductor's surface with oxygen vacancies (i.e., defective surface). Furthermore, by estimating the amount of charge transfer by varying the porphyrin-to-SnO$_2$ ratio, we demonstrated compelling proof that, at a fixed value of equivalent mass ratio, ZnTPP donates more electrons than the perfluorinated molecule, thus supporting the experimental materials' current values (recorded in air).

To dig deeper into the investigation, we also examined the impact of light by illuminating the samples during the sensing measurements using different light sources. No significant improvement could be noticed but, contrarily, a slight sensing worsening was observed in the case of ZnTPPF$_{20}$/SnO$_2$ 1:32 sample upon LED illumination (from 1.80 to 0.80 of signal's intensity at 20 ppm). Even in this case, the amount of electrons injected from porphyrins to SnO_2 CB plays a pivotal role since an overfilling of semiconductor's available states together with a greater electron scattering experimentally ends up being detrimental.

Lastly, by finely characterizing the most performing hybrids (i.e., 1:32 ratio), we successfully demonstrated the intimate contact between the adopted macrocycles and SnO_2 nanoparticles. Indeed, by means of FTIR, DRS, and HRTEM, we clearly noticed the materials' interaction, which we hypothesized to be physical in nature, also in accordance with the DFT investigation.

In conclusion, the take-home message of the present work is that achieving a balance between the porphyrin's electron injection and the available MOS states is crucial, whatever the chemiresistive mechanism is, herein, we embraced the most popular and widely accepted ionosorption model, and this balance can be achieved by customizing the chemistry of the porphyrins and adjusting the ratio between them and MOS. As such, herein, we showcased for the first time how to tailor the coupling of metal oxides with *ad hoc* Zn(II)-porphyrins, thus providing useful guidelines to achieve a boosted light-free gaseous sensing.

■ ASSOCIATED CONTENT

Data Availability Statement

All the data supporting the findings of this study are available within the article, in its Supporting Information, and from the corresponding author upon reasonable request.

SI Supporting Information

The Supporting Information is available free of charge at https://pubs.acs.org/doi/10.1021/acsami.4c05478.

> Gas sensing experimental setup (Figure S1); *I*−*V* curves (Figure S2); sensing responses of $ZnTPPF_{20}$ porphyrin and (b) $ZnTPPF_{20}/SnO_2$ 1:4 (Figure S3); comparison of responses obtained at dark and under UV or LED irradiations (Figure S4); charge transfer from ZnTPPs to the *n* unit cells competing to one admolecule (Figure S5); energetic, electronic, and structural data of acetone adsorption on SnO_2 (Table S1); ab initio optimized structures of acetone adsorbed on the (110) surface of SnO_2 (a) in the presence of an oxygen vacancy in the bulk, and (b) in the presence of an oxygen vacancy at both the surface (adsorption site) and in the bulk (Figure S6); neutral case (i.e., without additional electrons in the substrate), adsorption energies with respect to the molecular oxygen, charge state, and relevant atomic distances for the four oxygen species considered configuration (Table S2); charged case (i.e., with one additional electron in the substrate), adsorption energies with respect to the molecular oxygen, charge state, and relevant atomic distances for the four oxygen species/considered configuration (Table S3); the four different O adsorption configurations (Figure S7); XRPD patterns of SnO_2, $ZnTPP/SnO_2$ 1:32 and $ZnTPPF_{20}/SnO_2$ 1:32 (Figure S8); (a) UV/vis in CH_2Cl_2 solution, (b) TGA curves and (c) ^{1}H- and ^{19}F-NMR in $CDCl_3$ solution of pristine porphyrins (Figure S9); pores volume distribution by BET-BJH analysis (Figure S10); SEM micrographs of (a) pristine SnO_2, (b) $ZnTPP/SnO_2$ 1:32, (c) $ZnTPPF_{20}/SnO_2$ 1:32, (d) EDX spectrum of $ZnTPPF_{20}/SnO_2$ 1:32 (Figure S11) (PDF)

■ AUTHOR INFORMATION

Corresponding Author

Eleonora Pargoletti − *Dipartimento di Chimica, Università degli Studi di Milano, 20133 Milan, Italy; Consorzio Interuniversitario Nazionale per la Scienza e Tecnologia dei Materiali (INSTM), 50121 Florence, Italy;* orcid.org/0000-0003-4385-7461; Email: eleonora.pargoletti@unimi.it

Authors

Francesca Tessore − *Dipartimento di Chimica, Università degli Studi di Milano, 20133 Milan, Italy; Consorzio Interuniversitario Nazionale per la Scienza e Tecnologia dei Materiali (INSTM), 50121 Florence, Italy;* orcid.org/0000-0002-6691-0256

Gabriele Di Carlo − *Dipartimento di Chimica, Università degli Studi di Milano, 20133 Milan, Italy; Consorzio Interuniversitario Nazionale per la Scienza e Tecnologia dei Materiali (INSTM), 50121 Florence, Italy;* orcid.org/0000-0002-8782-7945

Cecilia Albanese − *Dipartimento di Chimica, Università degli Studi di Milano, 20133 Milan, Italy*

Raffaella Soave − *National Research Council of Italy, Institute of Chemical Sciences and Technologies "Giulio Natta", 20133 Milan, Italy*

Mario Italo Trioni − *National Research Council of Italy, Institute of Chemical Sciences and Technologies "Giulio Natta", 20133 Milan, Italy;* orcid.org/0000-0001-6165-1032

Federica Marelli − *Dipartimento di Chimica, Università degli Studi di Milano, 20133 Milan, Italy;* orcid.org/0009-0006-7054-6975

Giuseppe Cappelletti − *Dipartimento di Chimica, Università degli Studi di Milano, 20133 Milan, Italy; Consorzio Interuniversitario Nazionale per la Scienza e Tecnologia dei Materiali (INSTM), 50121 Florence, Italy;* orcid.org/0000-0002-1260-2979

Complete contact information is available at: https://pubs.acs.org/10.1021/acsami.4c05478

Author Contributions

Conceptualization: F.T., E.P., G.D.C., M.I.T., and G.C.; formal analysis: F.T., E.P., G.D.C., C.A., R.S., M.I.T., and F.M.; investigation: all authors; data curation: F.T., E.P, R.S., and M.I.T.; writing original draft: F.T., E.P. and R.S.; review and editing: G.D.C. M.I.T. and G.C.; supervision: F.T., E.P., G.D.C., and G.C.

Notes

The authors declare no competing financial interest.

■ ACKNOWLEDGMENTS

Part of this work was carried out at Unitech COSPECT and NOLIMITS, advanced imaging facility centres established by the Università degli Studi di Milano. Prof. Gian Luca Chiarello is gratefully acknowledged for the optimization of the gas sensing experimental setup. E.P. and G.C. would like to thank Prof. Alberto Vertova for the fruitful discussion about electrochemical characterization of the sensing materials and Prof. Mariangela Longhi for BET-BJH analyses. E.P. acknowledges the Italian Ministry of University and Research (MUR), National Recovery and Resilience Plan (NRRP)−Mission 4 "Education and Research"−Investment 1.2 "Funding projects presented by young researchers", financed by NextGenerationEU, project number SOE_0000117. E.P. kindly acknowledges University of Milan, Research Support Plan−Line 4, project number PSRL423EPARG_01. R.S. and M.I.T. acknowledge the CINECA award under the ISCRA initiative, for the availability of high-performance computing resources and support.

■ REFERENCES

(1) Yuan, Z.; Li, R.; Meng, F.; Zhang, J.; Zuo, K.; Han, E. Approaches to Enhancing Gas Sensing Properties: A Review. *Sensors* **2019**, *19* (7), No. 1495.

(2) Pargoletti, E.; Cappelletti, G. Breakthroughs in the Design of Novel Carbon-Based Metal Oxides Nanocomposites for VOCs Gas Sensing. *Nanomaterials* **2020**, *10* (8), No. 1485.

(3) Barandun, G.; Gonzalez-Macia, L.; Lee, H. S.; Dincer, C.; Güder, F. Challenges and Opportunities for Printed Electrical Gas Sensors. *ACS Sens.* **2022**, *7* (10), 2804−2822.

(4) Milone, A.; Monteduro, A. G.; Rizzato, S.; Leo, A.; Di Natale, C.; Kim, S. S.; Maruccio, G. Advances in Materials and Technologies for Gas Sensing from Environmental and Food Monitoring to Breath Analysis. *Adv. Sustainable Syst.* **2023**, *7* (2), No. 2200083.

(5) Zhu, L.; Zeng, W. Room-Temperature Gas Sensing of ZnO-Based Gas Sensor: A Review. *Sens. Actuators, A* **2017**, *267*, 242−261.

(6) Morsy, M.; Yahia, I. S.; Zahran, H. Y.; Meng, F.; Ibrahim, M. Portable and Battery Operated Ammonia Gas Sensor Based on CNTs/RGO/ZnO Nanocomposite. *J. Electron. Mater.* **2019**, *48* (11), 7328−7335.

(7) Pargoletti, E.; Verga, S.; Chiarello, G. L.; Longhi, M.; Cerrato, G.; Giordana, A.; Cappelletti, G. Exploring Sn$_x$Ti$_{1-x}$O$_2$ Solid Solutions Grown onto Graphene Oxide (GO) as Selective Toluene Gas Sensors. *Nanomaterials* **2020**, *10* (4), No. 761.

(8) Wei, Q.; Sun, J.; Song, P.; Yang, Z.; Wang, Q. Synthesis of Reduced Graphene Oxide/SnO$_2$ Nanosheets/Au Nanoparticles Ternary Composites with Enhanced Formaldehyde Sensing Performance. *Phys. E* **2020**, *118*, No. 113953.

(9) Kong, Y.; Li, Y.; Cui, X.; Su, L.; Ma, D.; Lai, T.; Yao, L.; Xiao, X.; Wang, Y. SnO$_2$ Nanostructured Materials Used as Gas Sensors for the Detection of Hazardous and Flammable Gases: A Review. *Nano Mater. Sci.* **2022**, *4* (4), 339−350.

(10) Tricoli, A.; Righettoni, M.; Teleki, A. Semiconductor Gas Sensors: Dry Synthesis and Application. *Angew. Chem., Int. Ed.* **2010**, *49* (42), 7632−7659.

(11) Pineau, N. J.; Kompalla, J. F.; Güntner, A. T.; Pratsinis, S. E. Orthogonal Gas Sensor Arrays by Chemoresistive Material Design. *Microchim. Acta* **2018**, *185* (12), No. 563.

(12) van den Broek, J.; Abegg, S.; Pratsinis, S. E.; Güntner, A. T. Highly Selective Detection of Methanol over Ethanol by a Handheld Gas Sensor. *Nat. Commun.* **2019**, *10* (1), No. 4220.

(13) Pargoletti, E.; Tricoli, A.; Pifferi, V.; Orsini, S.; Longhi, M.; Guglielmi, V.; Cerrato, G.; Falciola, L.; Derudi, M.; Cappelletti, G. An Electrochemical Outlook upon the Gaseous Ethanol Sensing by Graphene Oxide-SnO$_2$ Hybrid Materials. *Appl. Surf. Sci.* **2019**, *483*, 1081−1089.

(14) Zhang, S.; Zhang, B.; Sun, G.; Li, Y.; Zhang, B.; Wang, Y.; Cao, J.; Zhang, Z. One-Step Synthesis of Ag/SnO$_2$/RGO Nanocomposites and Their Trimethylamine Sensing Properties. *Mater. Res. Bull.* **2019**, *114*, 61−67.

(15) Zhang, L.; Khan, K.; Zou, J.; Zhang, H.; Li, Y. Recent Advances in Emerging 2D Material-Based Gas Sensors: Potential in Disease Diagnosis. *Adv. Mater. Interfaces* **2019**, *6* (22), No. 1901329.

(16) Wei, Q.; Sun, J.; Song, P.; Yang, Z.; Wang, Q. Synthesis of Reduced Graphene Oxide/SnO$_2$ Nanosheets/Au Nanoparticles Ternary Composites with Enhanced Formaldehyde Sensing Performance. *Phys. E* **2020**, *118*, No. 113953.

(17) Kim, N.-H.; Choi, S.-J.; Yang, D.-J.; Bae, J.; Park, J.; Kim, I.-D. Highly Sensitive and Selective Hydrogen Sulfide and Toluene Sensors Using Pd Functionalized WO$_3$ Nanofibers for Potential Diagnosis of Halitosis and Lung Cancer. *Sens. Actuators, B* **2014**, *193*, 574−581.

(18) Limosani, F.; Remita, H.; Tagliatesta, P.; Bauer, E. M.; Leoni, A.; Carbone, M. Functionalization of Gold Nanoparticles with Ru-Porphyrin and Their Selectivity in the Oligomerization of Alkynes. *Materials* **2022**, *15* (3), No. 1207.

(19) Bonin, J.; Maurin, A.; Robert, M. Molecular Catalysis of the Electrochemical and Photochemical Reduction of CO$_2$ with Fe and Co Metal Based Complexes. Recent Advances. *Coord. Chem. Rev.* **2017**, *334*, 184−198.

(20) Di Carlo, G.; Pizzotti, M.; Righetto, S.; Forni, A.; Tessore, F. Electric-Field-Induced Second Harmonic Generation Nonlinear Optic Response of A 4 β-Pyrrolic-Substituted Zn II Porphyrins: When Cubic Contributions Cannot Be Neglected. *Inorg. Chem.* **2020**, *59* (11), 7561−7570.

(21) Limosani, F.; Tessore, F.; Di Carlo, G.; Forni, A.; Tagliatesta, P. Nonlinear Optical Properties of Porphyrin, Fullerene and Ferrocene Hybrid Materials. *Materials* **2021**, *14* (16), No. 4404.

(22) Stoumpidi, A.; Trapali, A.; Poisson, M.; Barrozo, A.; Bertaina, S.; Orio, M.; Charalambidis, G.; Coutsolelos, A. G. Highly Efficient Light-Driven CO$_2$ to CO Reduction by an Appropriately Decorated Iron Porphyrin Molecular Catalyst. *ChemCatChem* **2023**, *15* (5), No. e202200856.

(23) Mathew, S.; Yella, A.; Gao, P.; Humphry-Baker, R.; Curchod, B. F. E.; Ashari-Astani, N.; Tavernelli, I.; Rothlisberger, U.; Nazeeruddin, M. K.; Grätzel, M. Dye-Sensitized Solar Cells with 13% Efficiency Achieved through the Molecular Engineering of Porphyrin Sensitizers. *Nat. Chem.* **2014**, *6* (3), 242−247.

(24) Li, L. L.; Diau, E. W. G. Porphyrin-Sensitized Solar Cells. *Chem. Soc. Rev.* **2013**, *42* (1), 291−304.

(25) Covezzi, A.; Biroli, A. O.; Tessore, F.; Forni, A.; Marinotto, D.; Biagini, P.; Di Carlo, G.; Pizzotti, M. 4D−π−1A Type β-Substituted Zn II -Porphyrins: Ideal Green Sensitizers for Building-Integrated Photovoltaics. *Chem. Commun.* **2016**, *52* (85), 12642−12645.

(26) Shen, J.; Wang, M.; Gao, J.; Han, H.; Liu, H.; Sun, L. Improvement of Electrochemical Water Oxidation by Fine-Tuning the Structure of Tetradentate N 4 Ligands of Molecular Copper Catalysts. *ChemSusChem* **2017**, *10* (22), 4581−4588.

(27) Biroli, A. O.; Tessore, F.; Di Carlo, G.; Pizzotti, M.; Benazzi, E.; Gentile, F.; Berardi, S.; Bignozzi, C. A.; Argazzi, R.; Natali, M.; et al. Fluorinated Zn II Porphyrins for Dye-Sensitized Aqueous Photoelectrosynthetic Cells. *ACS Appl. Mater. Interfaces* **2019**, *11* (36), 32895−32908.

(28) Berardi, S.; Caramori, S.; Benazzi, E.; Zabini, N.; Niorettini, A.; Biroli, A. O.; Pizzotti, M.; Tessore, F.; Di Carlo, G. Electronic Properties of Electron-Deficient Zn(II) Porphyrins for HBr Splitting. *Appl. Sci.* **2019**, *9* (13), No. 2739.

(29) Di Carlo, G.; Biroli, A. O.; Pizzotti, M.; Tessore, F. Efficient Sunlight Harvesting by A4 β-Pyrrolic Substituted ZnII Porphyrins: A Mini-Review. *Front. Chem.* **2019**, *7*, No. 177, DOI: 10.3389/fchem.2019.00177.

(30) Paolesse, R.; Nardis, S.; Monti, D.; Stefanelli, M.; Di Natale, C. Porphyrinoids for Chemical Sensor Applications. *Chem. Rev.* **2017**, *117* (4), 2517−2583.

(31) Belkova, G. V.; Zav'Yalov, S. A.; Glagolev, N. N.; Solov'Eva, A. B. The Influence of ZnO-Sensor Modification by Porphyrins on to the Character of Sensor Response to Volatile Organic Compounds. *Russ. J. Phys. Chem. A* **2010**, *84* (1), 129−133.

(32) Sivalingam, Y.; Martinelli, E.; Catini, A.; Magna, G.; Pomarico, G.; Basoli, F.; Paolesse, R.; Di Natale, C. Gas-Sensitive Photoconductivity of Porphyrin-Functionalized ZnO Nanorods. *J. Phys. Chem. C* **2012**, *116* (16), 9151−9157.

(33) Magna, G.; Muduganti, M.; Stefanelli, M.; Sivalingam, Y.; Zurlo, F.; Di Bartolomeo, E.; Catini, A.; Martinelli, E.; Paolesse, R.; Di Natale, C. Light-Activated Porphyrinoid-Capped Nanoparticles for Gas Sensing. *ACS Appl. Nano Mater.* **2021**, *4* (1), 414−424.

(34) Magna, G.; Catini, A.; Kumar, R.; Palmacci, M.; Martinelli, E.; Paolesse, R.; di Natale, C. Conductive Photo-Activated Porphyrin-

ZnO Nanostructured Gas Sensor Array. *Sensors* **2017**, *17* (4), No. 747.

(35) Ekrami, M.; Magna, G.; Emam-djomeh, Z.; Saeed Yarmand, M.; Paolesse, R.; Di Natale, C. Porphyrin-Functionalized Zinc Oxide Nanostructures for Sensor Applications. *Sensors* **2018**, *18* (7), No. 2279.

(36) Cho, B.; Lee, K.; Pyo, S.; Kim, J. Fabrication and Characterization of VOC Sensor Array Based on SnO_2 and ZnO Nanoparticles Functionalized by Metalloporphyrins. *Micro Nano Syst. Lett.* **2018**, *6* (1), No. 10, DOI: 10.1186/s40486-018-0072-3.

(37) Belkova, G. V.; Zav'Yalov, S. A.; Sarach, O. B.; Gulyaev, A. M.; Glagolev, N. N.; Solov'Eva, A. B.; Timashev, S. F. The Character of the Response of ZnO and SnO_2 Sensors Modified with Porphyrins to Volatile Organic Compounds. *Russ. J. Phys. Chem. A* **2008**, *82* (13), 2323−2328.

(38) Ongun, M. Z.; Oguzlar, S.; Erol, M. Effects of NiO, SnO_2, and Ni-Doped SnO_2 Semiconductor Metal Oxides on the Oxygen Sensing Capacity of H_2TPP. *Anal. Chim. Acta* **2022**, *1229*, No. 340387.

(39) Cho, B.; Lee, K.; Jo, E.; Kim, J. Detection of Mixed BTEX With Suppressed Reaction Specificity Using Tin Oxide Nanoparticles Functionalized by Multi-Metalloporphyrins. *IEEE Sens. J.* **2019**, *19* (24), 11791−11796.

(40) Xu, Y.; Zheng, L.; Yang, C.; Zheng, W.; Liu, X.; Zhang, J. Oxygen Vacancies Enabled Porous SnO_2 Thin Films for Highly Sensitive Detection of Triethylamine at Room Temperature. *ACS Appl. Mater. Interfaces* **2020**, *12* (18), 20704−20713.

(41) Righettoni, M.; Tricoli, A.; Gass, S.; Schmid, A.; Amann, A.; Pratsinis, S. E. Breath Acetone Monitoring by Portable Si:WO_3 gas Sensors. *Anal. Chim. Acta* **2012**, *738*, 69−75.

(42) Pargoletti, E.; Hossain, U. H.; Di Bernardo, I.; Chen, H.; Tran-Phu, T.; Chiarello, G. L.; Lipton-Duffin, J.; Pifferi, V.; Tricoli, A.; Cappelletti, G. Engineering of SnO_2−Graphene Oxide Nanoheterojunctions for Selective Room-Temperature Chemical Sensing and Optoelectronic Devices. *ACS Appl. Mater. Interfaces* **2020**, *12* (35), 39549−39560.

(43) Zhang, P.; Pan, G.; Zhang, B.; Zhen, J.; Sun, Y. High Sensitivity Ethanol Gas Sensor Based on Sn-Doped ZnO under Visible Light Irradiation at Low Temperature. *Mater. Res.* **2014**, *17* (4), 817−822.

(44) Pargoletti, E.; Hossain, U. H.; Di Bernardo, I.; Chen, H.; Tran-Phu, T.; Lipton-Duffin, J.; Cappelletti, G.; Tricoli, A. Room-Temperature Photodetectors and VOC Sensors Based on Graphene Oxide-ZnO Nano-Heterojunctions. *Nanoscale* **2019**, *11* (47), 22932−22945.

(45) Americo, S.; Pargoletti, E.; Soave, R.; Cargnoni, F.; Trioni, M. I.; Chiarello, G. L.; Cerrato, G.; Cappelletti, G. Unveiling the Acetone Sensing Mechanism by WO_3 Chemiresistors through a Joint Theory-Experiment Approach. *Electrochim. Acta* **2021**, *371*, No. 137611, DOI: 10.1016/j.electacta.2020.137611.

(46) Baur, W. H.; Khan, A. A. Rutile-Type Compounds. IV. SiO_2, GeO_2 and a Comparison with Other Rutile-Type Structures. *Acta Crystallogr., Sect. B: Struct. Crystallogr. Cryst. Chem.* **1971**, *27* (11), 2133−2139.

(47) Zhou, W.; Liu, Y.; Yang, Y.; Wu, P. Band Gap Engineering of SnO_2 by Epitaxial Strain: Experimental and Theoretical Investigations. *J. Phys. Chem. C* **2014**, *118* (12), 6448−6453.

(48) Soler, J. M.; Artacho, E.; Gale, J. D.; Garcia, A.; Junquera, J.; Ordejón, P.; Sánchez-Portal, D. The SIESTA Method for Ab Initio Order-N Materials Simulation. *J. Phys.: Condens. Matter* **2002**, *14* (11), No. 2745.

(49) Perdew, J. P.; Burke, K.; Ernzerhof, M. Generalized Gradient Approximation Made Simple. *Phys. Rev. Lett.* **1996**, *77* (18), No. 3865.

(50) Troullier, N.; Martins, J. L. Efficient Pseudopotentials for Plane-Wave Calculations. *Phys. Rev. B* **1991**, *43* (3), No. 1993.

(51) Ferreira, L. G.; Marques, M.; Teles, L. K. Approximation to Density Functional Theory for the Calculation of Band Gaps of Semiconductors. *Phys. Rev. B* **2008**, *78* (12), No. 125116.

(52) Ferreira, L. G.; Marques, M.; Teles, L. K. Slater Half-Occupation Technique Revisited: The LDA-1/2 and GGA-1/2 Approaches for Atomic Ionization Energies and Band Gaps in Semiconductors. *AIP Adv.* **2011**, *1* (3), No. 032119.

(53) Solomatin, M. A.; Radovic, M.; Petrunin, A. A.; Kirilenko, D. A.; Varezhnikov, A. S.; Dubourg, G.; Vasilkov, M. Y.; Bainyashev, A. M.; Nesterovic, A.; Kiselev, I.; et al. Towards Electronic Smelling of Ketones and Alcohols at Sub- and Low Ppms by Pinky-Sized on-Chip Sensor Array with SnO_2 Mesoporous Layer Gradually Engineered by near IR-Laser. *Chem. Eng. J.* **2023**, *474*, No. 145934.

(54) Al-Hashem, M.; Akbar, S.; Morris, P. Role of Oxygen Vacancies in Nanostructured Metal-Oxide Gas Sensors: A Review. *Sens. Actuators, B* **2019**, *301*, No. 126845.

(55) Liu, G.; Wang, Z.; Chen, Z.; Yang, S.; Fu, X.; Huang, R.; Li, X.; Xiong, J.; Hu, Y.; Gu, H. Remarkably Enhanced Room-Temperature Hydrogen Sensing of SnO_2 Nanoflowers via Vacuum Annealing Treatment. *Sensors* **2018**, *18* (4), No. 949, DOI: 10.3390/s18040949.

(56) De Lacy Costello, B. P. J.; Ewen, R. J.; Ratcliffe, N. M.; Sivanand, P. S. Thick Film Organic Vapour Sensors Based on Binary Mixtures of Metal Oxides. *Sens. Actuators, B* **2003**, *92* (1−2), 159−166.

(57) Wu, Q.; Feng, Z.; Wang, Z.; Peng, Z.; Zhang, L.; Li, Y. Visual Chemiresistive Dual-Mode Sensing Platform Based on SnS_2/Ti_3C_2 MXene Schottky Junction for Acetone Detection at Room Temperature. *Talanta* **2023**, *253*, No. 124063.

(58) Prabhu, N. N.; Shivamurthy, B.; Anandhan, S.; Rajendra, B. V.; Basanna, J. C. R.; Srivathsa, M. An Investigation on the Acetone and Ethanol Vapor-Sensing Behavior of Sol−Gel Electrospun ZnO Nanofibers Using an Indigenous Setup. *ACS Omega* **2023**, *8* (51), 49057−49066.

(59) Sopiha, K. V.; Malyi, O. I.; Persson, C.; Wu, P. Chemistry of Oxygen Ionosorption on SnO_2 Surfaces. *ACS Appl. Mater. Interfaces* **2021**, *13* (28), 33664−33676.

(60) Mäki-Jaskari, M. A.; Rantala, T. T. Band Structure and Optical Parameters of the SnO_2(110) Surface. *Phys. Rev. B* **2001**, *64* (7), No. 075407.

(61) Cox, D. F.; Fryberger, T. B.; Semancik, S. Oxygen Vacancies and Defect Electronic States on the SnO_2(110)-*1* × *1* Surface. *Phys. Rev. B* **1988**, *38* (3), No. 2072.

(62) Bader, R. Atoms in Molecules: A Quantum Theory. In *International Series of Monographs on Chemistry*; Oxford University Press: Oxford, 1990; Vol. *22*.

(63) Otero-de-la-Roza, A.; Johnson, E. R.; Luaña, V. Critic2: A Program for Real-Space Analysis of Quantum Chemical Interactions in Solids. *Comput. Phys. Commun.* **2014**, *185* (3), 1007−1018.

(64) Di Carlo, G.; Biroli, A. O.; Pizzotti, M.; Tessore, F.; Trifiletti, V.; Ruffo, R.; Abbotto, A.; Amat, A.; De Angelis, F.; Mussini, P. R. Tetraaryl Zn II Porphyrinates Substituted at *β*-Pyrrolic Positions as Sensitizers in Dye-Sensitized Solar Cells: A Comparison with Meso-Disubstituted Push-Pull Zn II Porphyrinates. *Chem. - Eur. J.* **2013**, *19* (32), 10723−10740.

(65) Malcıoğlu, O. B.; Bockstedte, M. Self-Metalation of a Free-Base Porphyrin on a Metal Oxide Surface Mediated by Extended Defects: Insight from Ab Initio Molecular Dynamics Simulations. *Surf. Sci.* **2022**, *723*, No. 122101.

(66) Gouterman, M. Spectra of Porphyrins. *J. Mol. Spectrosc.* **1961**, *6*, 138−163.

(67) Yuan, Y. J.; Tu, J. R.; Ye, Z. J.; Lu, H. W.; Ji, Z. G.; Hu, B.; Li, Y. H.; Cao, D. P.; Yu, Z. T.; Zou, Z. G. Visible-Light-Driven Hydrogen Production from Water in a Noble-Metal-Free System Catalyzed by Zinc Porphyrin Sensitized MoS_2/ZnO. *Dyes Pigm.* **2015**, *123*, 285−292.

(68) Guayaquil-Sosa, J. F.; Serrano-Rosales, B.; Valadés-Pelayo, P. J.; de Lasa, H. Photocatalytic Hydrogen Production Using Mesoporous TiO_2 Doped with Pt. *Appl. Catal., B* **2017**, *211*, 337−348.

(69) Rimoldi, L.; Meroni, D.; Pargoletti, E.; Biraghi, I.; Cappelletti, G.; Ardizzone, S. Role of the Growth Step on the Structural, Optical and Surface Features of TiO_2 Composites. *R. Soc. Open Sci.* **2019**, *6* (1), No. 181662, DOI: 10.1098/rsos.181662.